Fast Neutron Spectroscopy With Organic Scintillation Detectors in a High-Radiation Environment

B. Baramsai
HX5, LLC, Brook Park, Ohio

B.M. Steinetz
Glenn Research Center, Cleveland, Ohio

L. Forsley
JWK Corporation, Annandale, Virginia

R.E. Martin
Cleveland State University, Cleveland, Ohio

P.B. Ugorowski and M.D. Becks
HX5, LLC, Brook Park, Ohio

T.L. Benyo, A. Chait, R.C. Hendricks, and G.C. Fralick
Glenn Research Center, Cleveland, Ohio

N. Penney
Ohio Aerospace Institute, Brook Park, Ohio

V. Pines and M. Pines
PineSci Consulting, Avon Lake, Ohio

C.E. Sandifer II
Glenn Research Center, Cleveland, Ohio

NASA STI Program . . . in Profile

Since its founding, NASA has been dedicated to the advancement of aeronautics and space science. The NASA Scientific and Technical Information (STI) Program plays a key part in helping NASA maintain this important role.

The NASA STI Program operates under the auspices of the Agency Chief Information Officer. It collects, organizes, provides for archiving, and disseminates NASA's STI. The NASA STI Program provides access to the NASA Technical Report Server—Registered (NTRS Reg) and NASA Technical Report Server—Public (NTRS) thus providing one of the largest collections of aeronautical and space science STI in the world. Results are published in both non-NASA channels and by NASA in the NASA STI Report Series, which includes the following report types:

- TECHNICAL PUBLICATION. Reports of completed research or a major significant phase of research that present the results of NASA programs and include extensive data or theoretical analysis. Includes compilations of significant scientific and technical data and information deemed to be of continuing reference value. NASA counter-part of peer-reviewed formal professional papers, but has less stringent limitations on manuscript length and extent of graphic presentations.

- TECHNICAL MEMORANDUM. Scientific and technical findings that are preliminary or of specialized interest, e.g., "quick-release" reports, working papers, and bibliographies that contain minimal annotation. Does not contain extensive analysis.

- CONTRACTOR REPORT. Scientific and technical findings by NASA-sponsored contractors and grantees.

- CONFERENCE PUBLICATION. Collected papers from scientific and technical conferences, symposia, seminars, or other meetings sponsored or co-sponsored by NASA.

- SPECIAL PUBLICATION. Scientific, technical, or historical information from NASA programs, projects, and missions, often concerned with subjects having substantial public interest.

- TECHNICAL TRANSLATION. English-language translations of foreign scientific and technical material pertinent to NASA's mission.

For more information about the NASA STI program, see the following:

- Access the NASA STI program home page at http://www.sti.nasa.gov

- E-mail your question to help@sti.nasa.gov

- Fax your question to the NASA STI Information Desk at 757-864-6500

- Telephone the NASA STI Information Desk at 757-864-9658

- Write to:
  NASA STI Program
  Mail Stop 148
  NASA Langley Research Center
  Hampton, VA 23681-2199

Fast Neutron Spectroscopy With Organic Scintillation Detectors in a High-Radiation Environment

B. Baramsai
HX5, LLC, Brook Park, Ohio

B.M. Steinetz
Glenn Research Center, Cleveland, Ohio

L. Forsley
JWK Corporation, Annandale, Virginia

R.E. Martin
Cleveland State University, Cleveland, Ohio

P.B. Ugorowski and M.D. Becks
HX5, LLC, Brook Park, Ohio

T.L. Benyo, A. Chait, R.C. Hendricks, and G.C. Fralick
Glenn Research Center, Cleveland, Ohio

N. Penney
Ohio Aerospace Institute, Brook Park, Ohio

V. Pines and M. Pines
PineSci Consulting, Avon Lake, Ohio

C.E. Sandifer II
Glenn Research Center, Cleveland, Ohio

Acknowledgments

Available from

NASA STI Program
Mail Stop 148
NASA Langley Research Center
Hampton, VA 23681-2199

National Technical Information Service
5285 Port Royal Road
Springfield, VA 22161
703-605-6000

This report is available in electronic form at http://www.sti.nasa.gov/ and http://ntrs.nasa.gov/

Fast Neutron Spectroscopy With Organic Scintillation Detectors in a High-Radiation Environment

B. Baramsai
HX5, LLC
Brook Park, Ohio 44142

P.B. Ugorowski and M.D. Becks
HX5, LLC
Brook Park, Ohio 44142

B.M. Steinetz
National Aeronautics and Space Administration
Glenn Research Center
Cleveland, Ohio 44135

T.L. Benyo, A. Chait, R.C. Hendricks, and G.C. Fralick
National Aeronautics and Space Administration
Glenn Research Center
Cleveland, Ohio 44135

L. Forsley
JWK Corporation
Annandale, Virginia 22003

N. Penney
Ohio Aerospace Institute
Brook Park, Ohio 44142

R.E. Martin
Cleveland State University
Cleveland, Ohio 44115

V. Pines and M. Pines
PineSci Consulting
Avon Lake, Ohio 44012

C.E. Sandifer II
National Aeronautics and Space Administration
Glenn Research Center
Cleveland, Ohio 44135

Abstract

Organic scintillators with pulse shape discrimination capability are widely used in both research and practical applications of neutron detection. The neutron and γ-ray identification performance of the detector depends on the classification algorithms, noise filters and pileup rejection criteria in a high-flux bremsstrahlung radiation environment. In this paper, a technique has been developed and implemented for the neutron detection with multiple filter and discrimination steps, which to a high confidence level eliminates counting of γ-ray pulses. Such a technique is merited when making measurements in a high-flux bremsstrahlung and secondary fluorescence environment. The EJ-309 and stilbene detectors coupled to the digital data acquisition system were used for the calibration assessments with standard γ-ray and neutron sources such as ^{137}Cs, ^{60}Co, ^{252}Cf, and Am-Be. The MCNPX-PoliMi and GEANT4 toolkits were used to simulate the light output and the optical photon transport in the scintillators and create detector response functions for each type of detector. The neutron spectrum unfolding algorithm, GRAVELW, was used to recreate and calibrate with the Am-Be as the final step before applying the neutron detection system to extract fusion neutron spectra generated in an intense bremsstrahlung radiation environment. This new technique described offers the user the ability to measure neutron spectra in a high-flux γ-ray field and tune the parameters to meet required filtering needs.

1.0 Introduction

Neutron detectors principally work by indirect mechanisms such as neutron elastic scattering on light nuclei (p and d recoil) or nuclear reactions producing charged particles (α, p, and fission products, etc.). Reaction-based detectors use isotopes that have high thermal neutron cross sections. These types of detectors work efficiently, using neutron moderators to thermalize the incident neutrons, but as a consequence the neutron energy information is largely lost. Hence, recoil detectors are commonly used for fast neutron detection, as they preserve the spectroscopic information better than reaction-based detectors (Ref. 1).

In this work, EJ-309 liquid (manufactured by Eljen Technology) and stilbene crystal (Scintinel™ manufactured by Inrad Optics) organic scintillators were chosen for fast neutron detection. Both detectors have excellent pulse shape discrimination (PSD) capability (Refs. 2 and 3), and they have been used in moderately high γ-radiation environments (Refs. 4 and 5). Optimum digital pulse processing methodology coupled with signal filtering and PSD, as will be described, results in a high-fidelity technique that discriminates between neutrons and γ-rays and yields neutron spectral information.

Fast neutron spectroscopy is complicated since the incident neutrons do not deposit their full energy in a single collision within the detector volume and each detector material has its own characteristics. Therefore, careful detector response modeling is required to preserve the spectral information, as will be described in Section 2.2.

The neutron spectroscopic and unfolding techniques described herein have been used for neutron detection and diagnostics for bremsstrahlung-beam-initiated fusion experiments. The experimental facility, noteworthy fusion results, and physics of the experiments are described in separate papers (Refs. 6 and 7).

The purpose of the current paper is to illustrate the experimental and analytical procedures developed to extract neutron spectroscopic information and ensure proper discrimination between neutron and γ signals in a high-flux bremsstrahlung environment (estimated within the cave to be $\sim 3 \times 10^5$ γ/s/cm^2 at 2.9 MeV beam set point).

2.0 Test Measurements

Test measurements were performed with a relatively simple digital data acquisition system (DAQ) using a CAEN DT5730 desktop digitizer (Ref. 8). The D5730 is an 8-channel, 14-bit, 500 MS/s Desktop Waveform Digitizer with 2 Vpp (peak-to-peak) and 0.5 Vpp software-selectable input dynamics on single-ended MCX coaxial connectors. The detector's photomultiplier tube (PMT) anode signals are directly connected to the digitizer input. Using the digitizer DPP-PSD firmware, each detector's signals are triggered independently and recorded with CoMPASS (Ref. 8) readout software. Offline data analysis software was developed to extract and process the experimental information. Each triggered event contains information about channel number, trigger time-stamp, and waveform data with 2-ns sampling. The waveform length was set to about 400 ns long to cover the entire waveform and some baseline information. The DPP-PSD firmware has real-time pulse processing, filtering, and coincidence triggering options to reduce the readout throughput and write the most essential information. All events were recorded with waveforms and all signals were analyzed with the postprocessing software technique described herein.

2.1 Detector Calibration

In an organic scintillator, γ-rays are detected by recoiling atomic electrons through the Compton scattering mechanism, whereas neutrons are detected by recoil protons with elastic scattering. The number of optical photons produced for the recoiled charged particle with given energy is called light yield. Since electron light yield is linearly proportional to the electron energy, it is convenient to calibrate the scintillators' light yields in electron-equivalent units using standard γ-ray calibration sources. The proton light yield is not linear to the proton energy, and it is determined relative to the electron light yield, as will be discussed in Section 2.2. Compton scattering of a γ-ray from electrons generates continuous spectra, corresponding to energy depositions that depend on the scattering angle of the photon. Theoretically, the Compton spectrum has a sharp cutoff at the high-energy end, called the Compton edge, which corresponds to maximum energy deposition. The experimental spectrum has broadening due to the detector resolution. The energy resolution of the detector and position of the Compton edge were determined from coincidence measurements of the scintillators with a high-resolution lanthanum bromide (LaBr) detector.

The energy of a γ-ray after Compton scattering depends on scattering angle as represented in Equation (1).

$$E_f = \frac{E_i}{\dfrac{E_i}{m_e c^2}(1 - \cos\theta) + 1} \tag{1}$$

where E_i is the incident γ-ray energy, E_f is the scattered γ-ray energy, m_e is mass of an electron, c is the speed of light, and θ is the angle between incident and scattered γ-rays.

The LaBr detector was shielded and collimated with Pb blocks to detect γ-rays scattered off from the stilbene (or EJ-309) detector in coincidence. Changing relative positions of the detectors and the source, the coincidence spectrum measures Compton energy depositions, $E_i - E_f$, in the scintillator as well as scattered γ-ray energy, E_f, in the scintillator. Figure 1 shows coincidence spectra for the case of 180° Compton backscattering when the highest energy deposition occurs in the scintillator. Using Equation (1) it is determined that 661.7-keV γ-rays from a ^{137}Cs source deposit 477.4 keVee in the scintillator and 184.3 keV in the LaBr detector.

The coincidence energy spectrum determines the resolution of the scintillator and the location of the Compton edge. Energy resolution is expressed with the following relation (Ref. 1):

$$\frac{\Delta E}{E} = \sqrt{A^2 + \frac{B^2}{E} + \frac{C^2}{E^2}} \tag{2}$$

where ΔE is the full width at half maximum (FWHM) of the coincidence peak, and the A, B, and C coefficients are determined using a multiparameter curve fit of the experimental resolution at various energies, as in Table I.
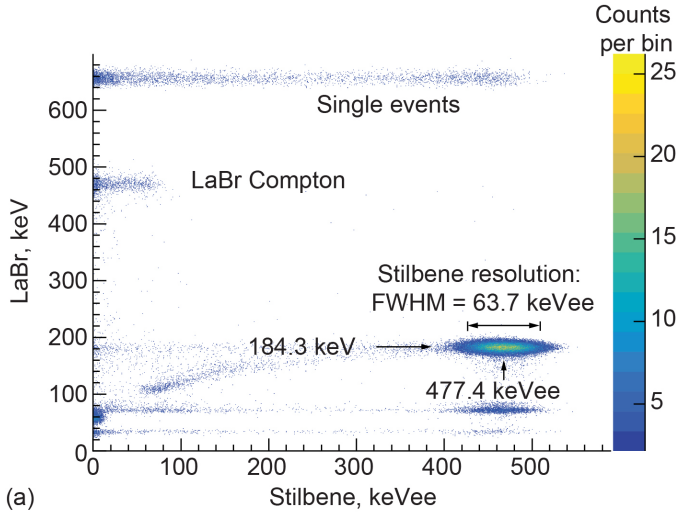
(a)
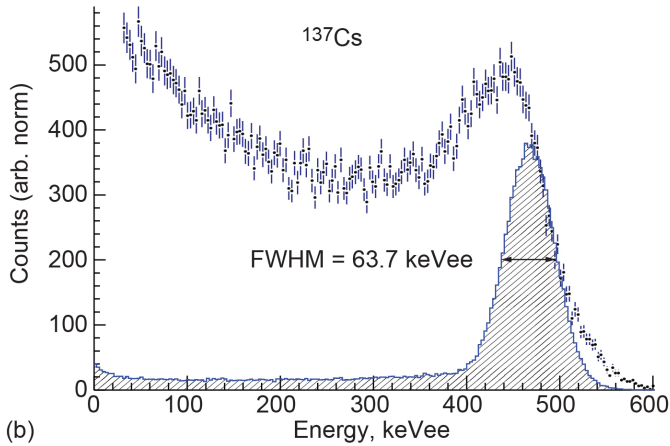
(b)

Figure 1.—LaBr and stilbene coincidence spectra for the case of 180° Compton backscattering. (a) LaBr versus stilbene two-dimensional (2-D) spectra. FWHM is the full width at half maximum. (b) Comparison of ^{137}Cs single-hit spectrum and the coincidence spectrum (striped area) that is created by projecting the 2-D spectrum around 183±10 keV energy bins.

TABLE I.—ENERGY RESOLUTION COEFFICIENTS OF THE SCINTILLATORS

Scintillator	A	B, keV$^{1/2}$	C, keV
Stilbene	0.05±0.02	3.0±1.0	26.4±4.2
EJ-309	0.06±0.03	3.1±1.0	24.5±4.0

The coincidence spectra were measured with a ^{137}Cs source at 30°, 40°, 60°, 80°, 100°, and 180°, and with a ^{60}Co source at 180°. The resolution coefficients for the stilbene and EJ-309 detectors are determined by fitting the resolution plot from the coincidence data. The coefficients were used in the MCNPX-PoliMi postprocessing code to create the detector response matrix.
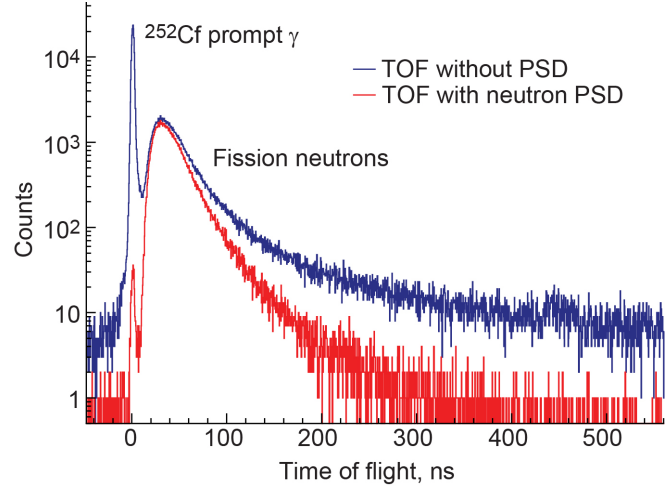

Figure 2.—^{252}Cf time of flight (TOF) spectra with and without pulse shape discrimination (PSD).

The resolution coefficients do not represent the intrinsic resolution of the detectors. The coefficients' uncertainties are relatively large, due to various factors such as goodness of the fit, coincidence peak broadening related to the detector size (solid angle to observe the scattering photon), and Doppler broadening and electronic noise of the acquisition system, etc.

As shown in the bottom panel of Figure 1, the Compton edge location is roughly about two-thirds of the Compton peak height. Alternatively, Safari et al. showed that the half value (or some other percent) of the peak height could not be considered as a universal measure of the Compton edge (Ref. 9). The local maximum of the Compton spectrum peak height shifts to the left-hand side of its original (correct) position, depending on the resolution. In this paper, the Compton edge position is defined for calibration purposes by adding $(1/2)\sigma$ of Gaussian fit of the Compton spectra to the peak center.

2.2 Light Output Relation

Proton recoil light output is well studied for the EJ-309 scintillator (Refs. 10 and 11), whereas stilbene scintillator data are not abundant. Therefore, the stilbene response for proton recoils was calibrated using the neutron time of flight (TOF) method when exposed to a ^{252}Cf fission neutron source as shown in Figure 2.

Approximately 80 h of data were collected with the source activity of 1.01×10^5 n/s (23 μCi) to get coincidence TOF spectrum with sufficient statistics.

Neutron energy is determined by the TOF over a distance of 0.45 m between the source and detector with a simple nonrelativistic relation for ^{252}Cf spontaneous fission neutrons. The TOF is determined by the time difference between the pulses triggered within a 2-μs coincidence window between the

fission tagging detector (EJ-200), located near the source, and the selected scintillator. High-precision time is calculated by the digital constant fraction discrimination (CFD) technique.

Neutron pulse-height spectra in electron-equivalent units are created with selected neutron energy gates to determine the relationships between electron and proton light outputs as a function of neutron energy ($L(E_n)$). This relation is represented with the following commonly used formula, Equation (3), that is presented by Cecil et al. (Ref. 12) and found in additional recent publications (Refs. 10, 11, and 13):

$$L(E_n) = AE_n - B\left(1 - e^{-CE_n^D}\right) \qquad (3)$$

where the A, B, C, and D coefficients are determined by fitting the TOF data with the relations described above. The fitting procedure used was the same as that used by Enqvist et al. (EJ-309) (Ref. 10): fixing the coefficient in the exponent, D, equal to one that gives better R^2 of the fit and good agreement with previous works.

Table II compares the fit results with other references for the EJ-309 scintillator. The empirical formula represents the locus of the response matrix that spans the end points of the neutron pulse-height spectrum at different energies.

Monte-Carlo-based MCNPX-PoliMi (Ref. 14) and GEANT4 (Ref. 15) simulations were used to create the detector response matrix for incident neutrons. The 10^8 particles were utilized in each 50-keV energy bin ranging from 100 keV to 15 MeV. This maintained the statistical uncertainty to less than 1 percent. The EJ-309 detector response matrix simulation is shown in Figure 3, and similar results were obtained with the stilbene detector as well.

The MCNPX-PoliMi Monte Carlo software simulates neutron and γ-ray transport through the detector volume. Collisions of source particles in the detector cells are stored in a collision output file containing detailed information about each collision, including the particle energy, collision nucleus, and time of collision after the source event.

The MPPost (Ref. 14) postprocessing code converts the collision output files into the detector response function. MPPost has built-in response functions for commonly used detectors, including the organic scintillators. Light output is calculated from the energy transfer of incident particles according to the particle type and collision nucleus. The energy resolution of the detector is calculated with Equation (3).

In the GEANT4 simulation, the scintillation light output is modeled by the semi-empirical Birk's formula. The Birk's coefficient is set in the detector construction class as a scintillator property. A good description of the GEANT4 simulation of organic scintillators is given in Ref. 16. The

TABLE II.—COEFFICIENTS OF LIGHT OUTPUT RELATION BETWEEN ELECTRON AND PROTON ENERGY DEPOSITIONS, INCLUDING 1-σ UNCERTAINTIES
[Detector sizes: EJ-309 (50 by 75 mm) and stilbene (25 by 25 mm).]

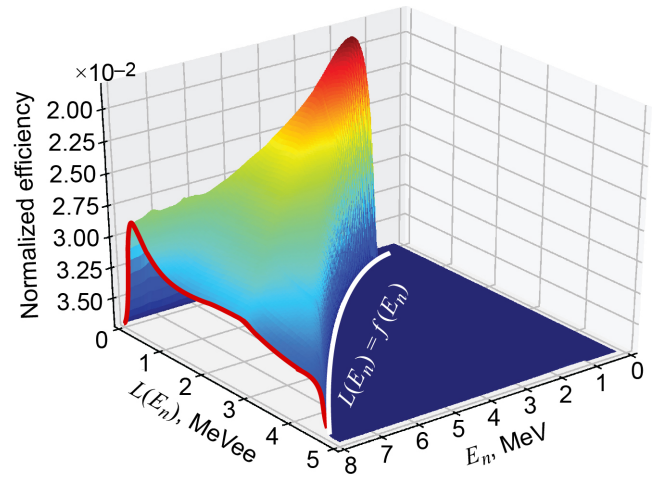| Reference	A, MeVee/MeV	B, MeVee	C, MeV^{-1}	D
This work (stilbene)	0.63±0.05	2.1±0.5	0.27±0.03	1.0
This work (EJ-309)	0.95±0.06	4.7±0.5	0.22±0.04	1.0
Pino et al. (Ref. 11) (EJ-309)	0.62±0.03	1.3±0.3	0.39±0.08	0.97
Enqvist et al. (Ref. 10) (EJ-309)	0.95±0.06	4.7±0.5	0.22±0.04	1.0

Figure 3.—Light output response function of EJ-309 detector simulated with MCNPX-PoliMi code for monoenergetic neutrons step by step from 0.5 MeV to 10 MeV. Solid white line, $L(E_n) = f(E_n)$ where $L(E_n)$ is the light output and E_n is neutron energy, shows the conversion function represented by Equation (3) that connects the points at the high-energy end of the pulse-height spectrum. The bold red line highlights a pulse-height spectrum for 8-MeV neutrons.

G4EmSaturation method is used to simulate the Birk attenuation in the optical physics class. Birk's constant (k_B) is set at 0.126 and 0.163 mm/MeV for the EJ-309 and stilbene detectors, respectively. Additional material properties of the scintillator, such as elemental compositions and density, are determined in materials definition cards in both MCNPX and GEANT4. GEANT4 has more detailed optical photon simulations, including fast and slow scintillation decay times, yield ratio, reflection and refraction indices of the scintillator medium and container walls, etc. The following mandatory and user action classes were utilized for the simulation: the DetectorConstruction class defines the detector constructions, geometries, and materials properties; the PhysicsList class

defines particles and physical processes to be taken into account; the *PrimaryGeneratorAction* and *ParticleGun* classes generate primary particles and direction; and the *SteppingAction*, *EventAction*, and *RunAction* classes track the particles and score events information.

2.3   Efficiency

Theoretically, neutron detection efficiency ϵ_{max} can be estimated from the following relation of neutron interaction probability in the scintillator volume:

$$\epsilon_{max} = 1 - e^{-N_H \sigma_{el} x} \qquad (4)$$

where N_H is the number density of hydrogen atoms in the scintillator, σ_{el} is the elastic scattering cross section of neutrons on the hydrogen and x is the detector size (length) along the particle direction. The number density of the hydrogen atoms is 5.43×10^{22} atoms/cm^3 for EJ-309 and 4.62×10^{22} atoms/cm^3 for stilbene. The neutron elastic scattering cross section is about 15 barn at 50 keV and decreases to 1 barn at 10 MeV. Hence, it is evident that the efficiency of detecting high-energy neutrons decreases as energy increases. Alternatively, the neutron detection threshold is defined by the minimum proton recoil energy that results in scintillation. As shown by the simulations in Figure 4, the efficiency is smaller as the threshold E_{thr} increases. Comparisons of the simulations for the different-sized detectors are also shown.

Efficiencies of the detectors are determined experimentally by comparing the TOF spectra with the reference ^{252}Cf fission neutron spectrum (Ref. 17) and the simulations. As demonstrated by Gonnenwein et al. (Ref. 18), the ^{252}Cf neutron spectrum in the Lab reference frame is well described by a Maxwell distribution at temperature $T = 1.42$ MeV (Ref. 18). Simulated neutron-energy-dependent efficiencies of the detectors compared with the experimental spectrum are shown in Figure 4. Average efficiencies are determined from the experiments with the Am-Be and the ^{252}Cf sources simply with the ratio of the number of detected neutrons and estimated number of neutrons hitting the detector. The Am-Be source activity is 40 mCi (8.8×10^4 neutron/s), and the ^{252}Cf source activity is 23 μCi (1.01×10^5 neutron/s). The average efficiencies are calculated as 12.6 ± 0.5 percent for the stilbene at the threshold $E_{thr} = 0.1$ MeVee and 23.4 ± 0.5 percent for the EJ-309 at the threshold $E_{thr} = 0.2$ MeVee. Approximate average and maximum neutron energies for each of the sources are as follows: ^{252}Cf = 2.1 MeV (with >10 MeV max.) and Am-Be = 4.2 MeV (with 11 MeV max.).
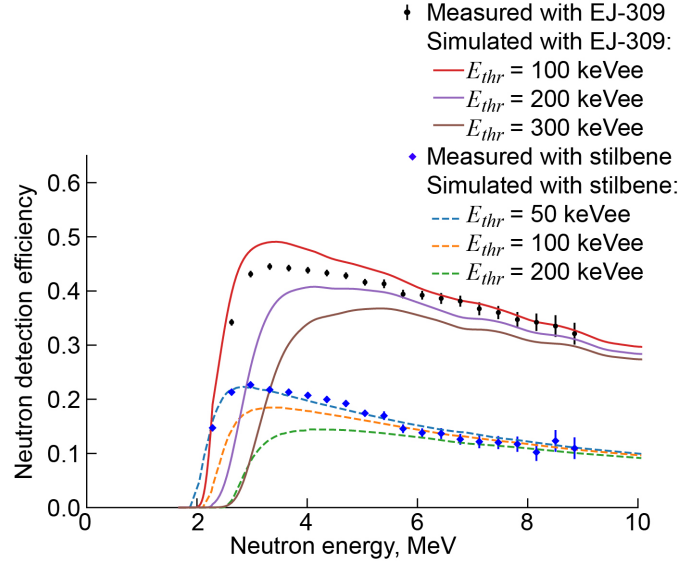

Figure 4.—^{252}Cf Neutron detection efficiency of large 50- by 75-mm EJ-309 detector and small 25- by 25-mm stilbene detector at different thresholds, E_{thr}.

Actual detection efficiency is smaller than the simulated absolute efficiency depending on the data reduction cuts discussed in Section 3.0. Experimental thresholds of the detectors are determined by the minimum amplitude of the signal to record, which was set as the analog-to-digital converter (ADC) trigger parameter. Further adjustment (increase) of the threshold is needed, depending on the neutron and γ-ray PSD capability near the threshold. The stilbene detector has a better PSD performance, which starts separating neutron and γ-ray pulses at about 60 ± 15 keVee and above, and the EJ-309 detector needs a higher threshold of about 150 ± 30 keVee and above. In a high-radiation environment, the PSD distributions near the threshold become wider, and the clean separation between the neutron and γ-ray pulses starts at about 100 ± 20 keVee for the stilbene and 300 ± 50 keVee for the EJ-309 detector. Figure 5 illustrates the PSD and the figure of merit (FOM) of the detectors near the threshold using Am-Be + ^{137}Cs source data.

3.0   Noise and Pileup Cleaning

3.1   Noise Filters

Two stages of data analysis software have been developed. In the first stage, the software reads and processes the signal waveforms, calculates basic parameters, and writes them into a compact size binary file format for faster subsequent processing. In this stage of the analysis, the software writes the
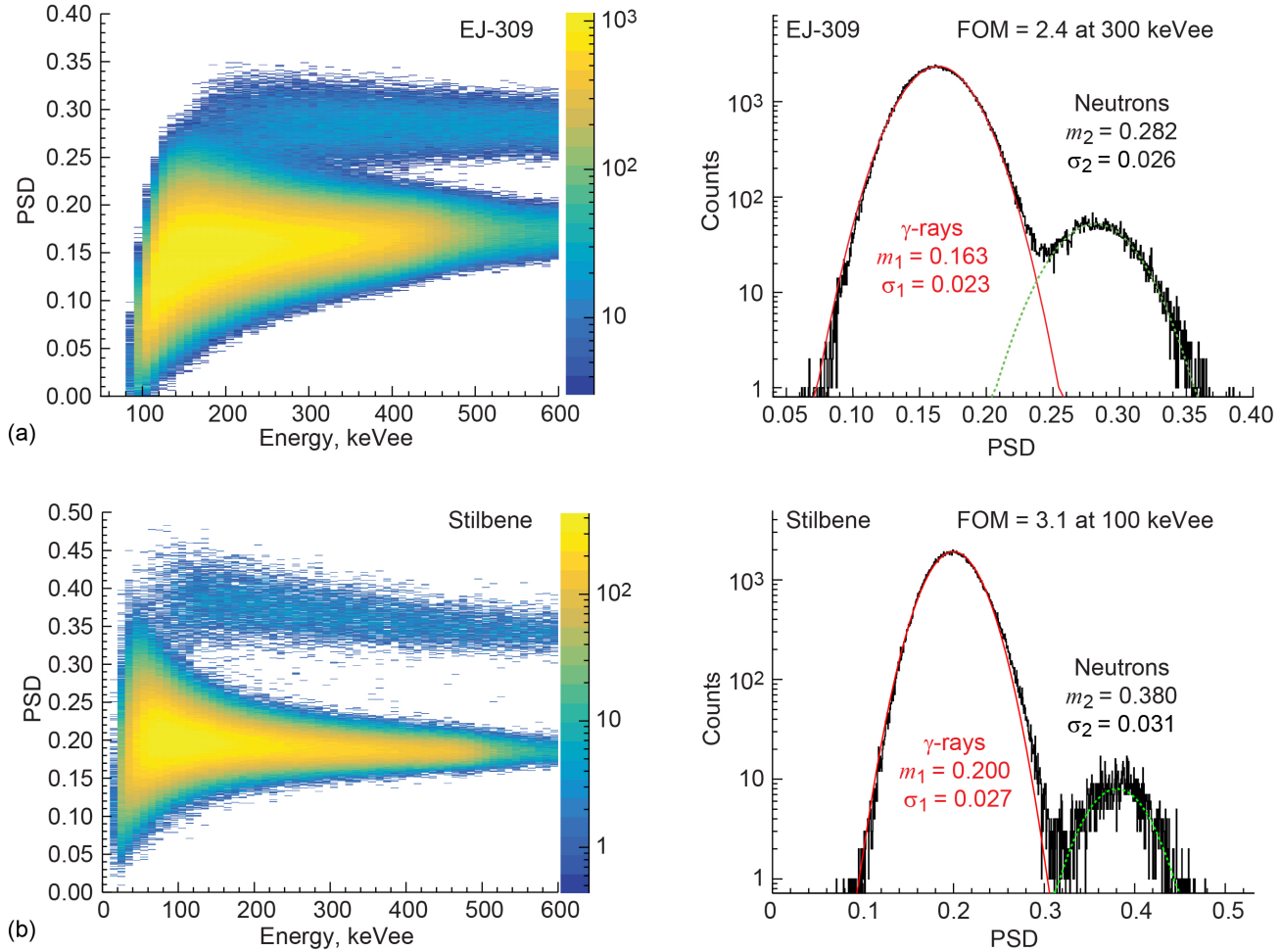
Figure 5.—Pulse shape discrimination (PSD) of (a) EJ-309 and (b) stilbene detectors and corresponding figures of merit (FOMs) near the threshold electron-equivalent energies. Mean values m_i and standard deviations σ_i are given for both γ-ray and neutron signals.

baseline integral, baseline root mean square (RMS), and baseline-subtracted short and long integrals of the signal. It also generates distributions of baseline mean, baseline RMS, and template matching. In the second stage, each of the signal parameters are compared with the distributions built from the first stage and filtered as a clean (noise-free) signal. The digitizer DPP-PSD firmware (CAEN S.p.A) makes onboard calculations of the quantities specified in the first stage, but the entire waveform was acquired to implement customized noise and pileup filters, as will be described next.

3.2   Baseline RMS

One of the quantities measured was the noise defined as the RMS of the baseline in the pretrigger portion of the recorded waveforms, set at 264 ns. Thirty-two samples (64 ns) were collected before the trigger point for the baseline calculation. This method allows the baseline stability and baseline RMS to be evaluated in a noisy environment containing both the high-flux γ-rays as well as x-ray fluorescence. If there were small signals (spikes) below the detection threshold before the triggered signal, both the baseline integral and oversubtraction of the integrals were bigger. The probability of such events is not small for the bremsstrahlung beam experiments, since the bremsstrahlung radiation yield rapidly increases toward the low-energy end. Baseline RMS distribution is very narrow, and signals >5 standard deviations from the mean RMS were rejected; that is, about 0.4 mV out of a 2-V dynamic range.

3.3   Baseline Shift

The trigger holdoff parameter was set at 400 ns, long enough to allow decay of the previously triggered signal and prevent retriggering the next signal on the tail of the previous signal. However, a small portion of data was observed to have slightly shifted average baseline positions in the noisy environment.

This could be an indication of a baseline restoration issue of the ADC, where the scintillator glows because of the high radiation rate or triggering on the tail of the previous pulse. On closer inspection, the baseline was found to be stable most of the time during the experiments. To be conservative, the signals were cleared out with baseline averages shifted by 20 or more LSBs (least significant bits) from the distribution mean.

3.4   Template Matching

Similar to Bourne et al. (Ref. 19), template-matching pulse filters were used to distinguish between neutron and γ-ray pulses. Figure 6 illustrates the comparison of a signal waveform with the average neutron and γ-ray templates that were built from the ^{252}Cf source spectra. The K-nearest neighbor approach was used to build the distributions of distances from the template. Euclidean distance between the measured pulse and the template is calculated:

$$\text{Distance}(d) = \sqrt{\sum_{i=N_{\text{sample}}} \left(t_i - s_i \right)^2} \qquad (5)$$

where t_i and s_i are the template and signal amplitudes at sample i normalized to the amplitude maximum. This technique generates two Gaussian distributions for the signals, allowing comparison with the neutron and γ-ray templates. The filter accepts the signal as a good signal if the template distance is within 3σ integral of neutron or γ-ray distributions. The filter was able to be customized to prioritize neutron or γ-ray signals only, as a PSD filter. However, the template-matching method needed to be augmented with the charge integral method described in Section 4.0.

3.5   Pileup Detection

As discussed in Reference 19, the rate-dependent pileup probability is estimated with

$$\text{Pileup probability} = 1 - e^{-\mu t} \qquad (6)$$

where μ is the count rate and t is the record length, which was selected as 400 ns.

The pileup rate is less than 1 percent of the events for rates up to 25 kHz and increases to 13 percent at a signal rate of 350 kHz, which was the highest radiation rate tested. To retain high data quality, radiation levels were limited so that the sampling rate was less than 25 kHz per channel. For the radiation source measurements, the count rate was controlled by changing the distance between the detectors and the source.
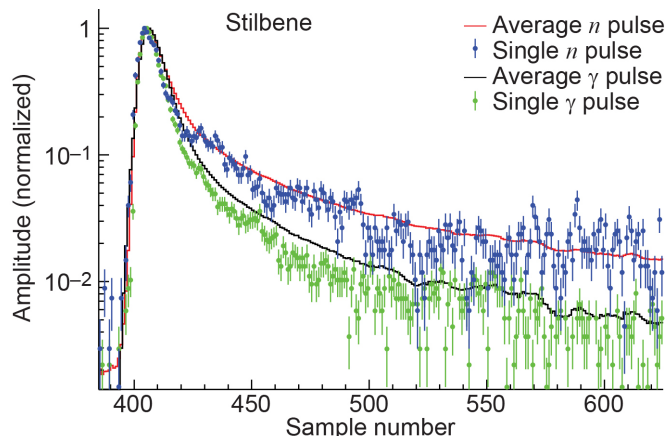

Figure 6.—^{252}Cf neutron and γ-ray signatures recorded using stilbene and the ADC. Time (ns) = 2 × sample number. Note: The average pulse is created adding 10,000 single pulses and normalized the peak value to 1. So, a given single pulse can deviate from the average.

For the bremsstrahlung beam experiments, it was reduced with the Pb cave shielding.

The pileup probability estimated by Equation (6) is the probability of simultaneous hits of two different particles in the detector. For the large-size detector (EJ-309), it is also possible that the same neutron generates multiple hits with two or more scatterings within the detector volume and creates "pileup-like" signals. The mean free path ($\lambda = 1/(\rho\sigma_{el})$, where ρ = number density and σ_{el} = elastic scattering cross section) in the scintillators is roughly 1.5 to 20 cm for neutrons with energies from 0.5 to 10 MeV, respectively. However, for those high-energy neutrons, the average flight time between the two consecutive hits is about 2 to 5 ns, which is about the same as the ADC sampling time, 2 ns. At lower energies of 10 to 100 keV, the mean free path is about 1.2 cm, and the time between hits is about 9 ns. Therefore, it is possible for neutrons moderating in the scintillator volume to generate small spikes on the tail of the main signal. The GEANT4 simulation of neutron elastic scattering in the scintillator confirms that the neutron moderation events are not negligible. The time between two consecutive scatterings of γ-rays are fractions of ns, which is below the ADC sampling time, so they do not create pileup-like signals.

The peak detection algorithm within the CERN ROOT data analysis framework was used to detect signal pileup peaks. The function takes two arguments: (1) minimum amplitude of the pileup peak to detect and (2) the time resolution of the peaks. The time resolution was set to 0.5 ns and the threshold was set at different values from 0.05 to 10 percent to find the optimum value. Pileup is detected if the value in the center of the peak value "i" minus the average value in two symmetrically positioned channels (channels i–3σ, i+3σ) is greater than a

preset threshold. Another relatively simple, fractional peak detection algorithm is introduced by Bourne et al. (Ref. 19). Both methods gave similar results at the same thresholds, corroborating the method used.

Figure 7(a) shows the detected pileup signal fractions for different types of sources (e.g., natural sources or bremsstrahlung beam radiation + D–D fusion) with different ADC rates. It is evident that for a given case, the detected pileup signal is almost constant at thresholds between 1 to 5 percent and then decreases above 5 percent. The fraction of pileup signal increases sharply for the thresholds below 1 percent. Figure 7(b) shows the results of the sensitivity study investigating the effects of the chosen pileup threshold percentages for the ^{252}Cf source and the EJ-309 detector, plotting neutron counts versus electron-equivalent energy. Again, the overall spectral shape is consistent for the thresholds above 1 percent. The low-energy counts in the spectrum reduce as the threshold increases, revealing that "good" neutron signals are also removed with pileup rejection. Especially for the small-amplitude signals, a few percent of threshold could eliminate good signals.

The optimum threshold value is set at 5 percent for the calibration source measurements that reduces pileup while letting more signals in. Due to the fact that bremsstrahlung radiation yield rapidly increases toward the low-energy end and the presence of secondary fluorescence in the Pb cave, we set the threshold at 0.8 percent to reduce those low-energy spikes without altering the spectral shape too much. Figure 7(c) shows the ^{252}Cf spectrum for the stilbene detector.

4.0 PSD Algorithms

Many different methods are used for PSD, as are illustrated in Refs. 20 and 21 and referenced therein. Many of those methods are based on the scintillation decay time differences of the neutron and γ-ray pulses. Figure 6 shows average neutron and γ-ray pulses compared with single pulses. As shown in the plot, light pulses for γ-rays are shorter than for neutrons, which gives the PSD capability. The manufacturers' data sheets indicates the decay constants of the scintillators are 3.5 and 4.5 ns for EJ-309 and stilbene, respectively (Refs. 2 and 3), which indicates the fast fluorescence decay time for stilbene is slightly longer. Iwanowska et al. (Ref. 22) fit the light-pulse shapes for γ-rays and neutrons using exponential curves with three separate components: slow, medium, and fast. They extracted the fast, medium, and slow decay time constants for EJ-309 as 3.7, 31, and 140 ns, respectively, for γ-rays, and the corresponding time constants for neutrons were 4.8, 32, and 140 ns. For γ-rays, 80 percent of the scintillation
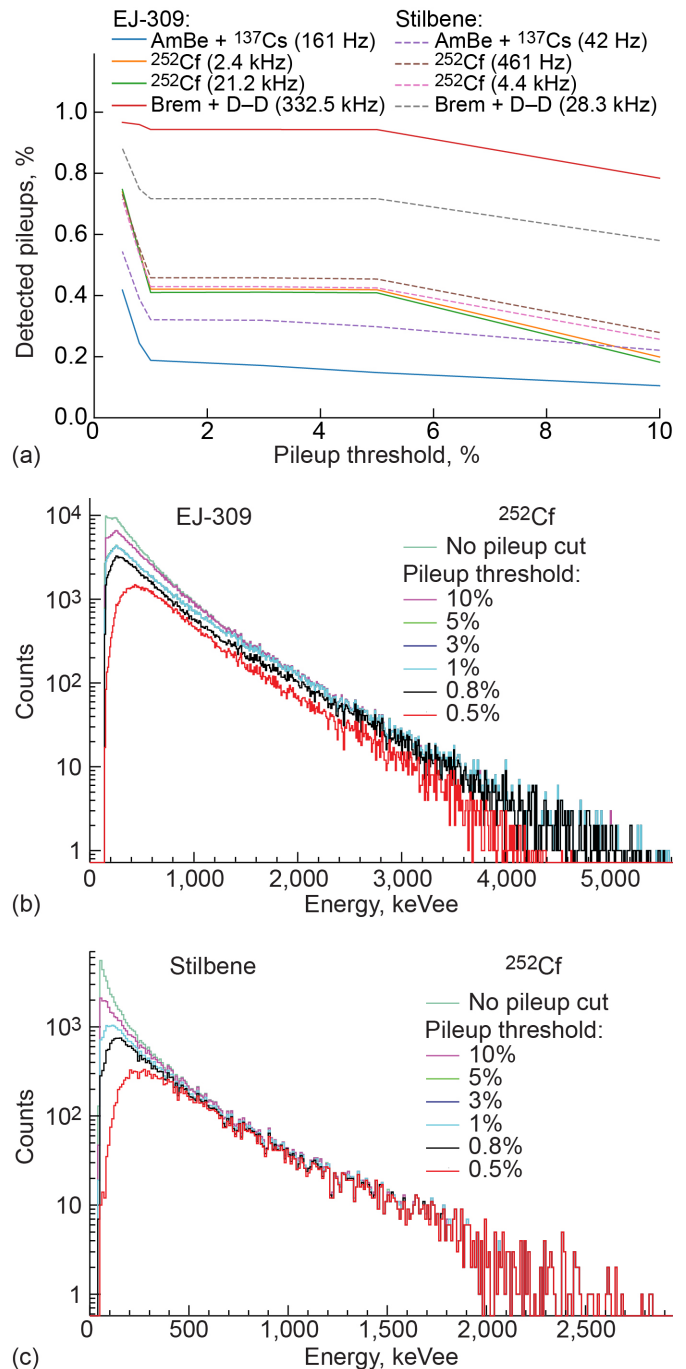

(a)

(b)

(c)

Figure 7.—Detector pileup response. (a) Detected pileups for both EJ-309 and stilbene for various sources (AmBe + ^{137}Cs, ^{252}Cf, and bremsstrahlung + D–D fusion). (b) Effect of threshold on EJ-309 spectrum. (c) Effect of threshold on stilbene spectrum. Note the spectrum for 1, 3, and 5 percent thresholds are close to one another and so are not discernible on the log scale.

light intensities are in the fast component and 20 percent are in the medium and slow components. For neutrons, the intensities are 46 percent in the fast component and 54 percent for the medium and slow components.

Intervals of 36 and 48 ns were used for the fast integrals for stilbene and EJ-309 scintillators over a range of 280 ns. The PSD parameter is measured with the ratio of tail-to-total integrals. Generally, the neutron and γ-ray pulse separation FOM for the stilbene detector was found to be better than that for the EJ-309 FOM (Ref. 20). For this environment, the PSD boundary between neutrons and γ-rays was set with high confidence by fitting the γ-ray PSD distribution with a Gaussian and setting the edge of the neutron gate as the mean + 8σ (where 8σ corresponds to 1 part in 1.6×10^{15}). The PSD distribution in Figure 8(a) shows the PSD plot of the stilbene detector for a bremsstrahlung beam experiment, with the neutron gate drawn with the 8σ criteria. Similar results were obtained for the EJ-309 detector, as shown in Figure 9(a).

Figure 8(b) shows a neutron pulse-height spectrum of neutrons with the PSD gate. The experimental pulse-height spectrum is compared with the simulated spectrum for monoenergetic neutron energies of 2.5, 4.0, and 7.5 MeV. The simulated stilbene spectra for the monochromatic neutron energies are scaled up by 12,000 for E_n = 2.5 MeV, 1,500 for E_n = 4.0 MeV, and 1,500 for E_n = 7.5 MeV. The simulated EJ-309 spectrum (Figure 9(b)) for the monochromatic neutron energies is scaled up by 18,500 for E_n = 2.5 MeV, 6,000 for E_n = 4.0 MeV, and 2,000 for E_n = 8.0 MeV for comparison with the experimental data.

As can be seen from the plot, the experimental data show evidence of D–D fusion events producing 2.5-MeV neutrons and higher energy neutrons boosted by the other mechanisms described in the previous papers (Refs. 6 and 7). Figure 8(c) shows the result of the spectrum-unfolding algorithm GRAVELW (Ref. 23) used to create the neutron energy spectrum from the pulse-height spectrum. The unfolded result shows a spectrum with fusion and higher energy neutrons. Figure 9(c) shows similar results that were obtained for the EJ-309 detector, and because of its larger size, could better resolve the higher energy neutrons.

5.0   Measurement Uncertainty

The uncertainty bars for the neutron spectra in Figure 8(c) and Figure 9(c) were determined based on the combined effect of detector energy resolution and the unfolding algorithm. The neutron energy uncertainties (horizontal bars) were determined using the perturbation method. First, the standard deviation in electron-equivalent units was determined by examining the response of the detectors to established γ-ray peaks for
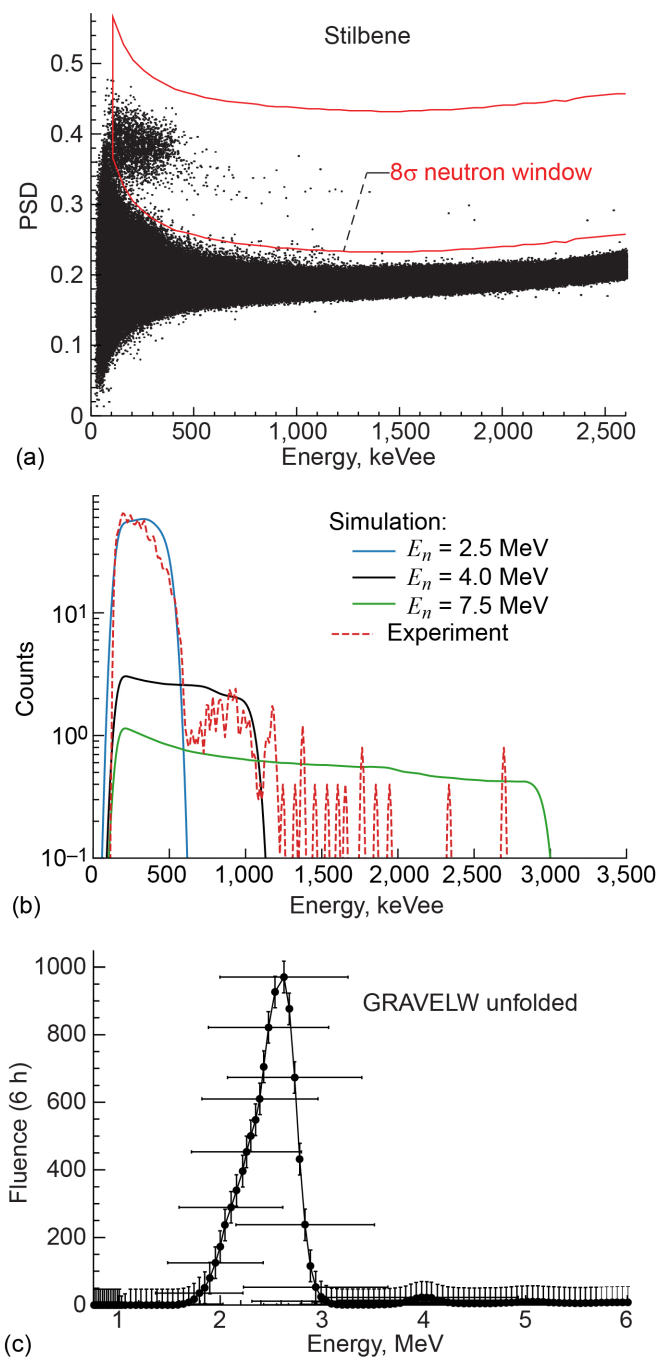

(a)

(b)

(c)

Figure 8.—Stilbene detector results: (a) experimental pulse shape discrimination (PSD) plot; (b) comparison of simulated monochromatic neutron flux with energies E_n of 2.5 MeV (fusion), 4.0 MeV, and 7.5 MeV simulated spectra versus experimental data from Ref. 6; (c) GRAVELW (Ref. 23) unfolded spectrum for representative experimental data from Ref. 6 where the uncertainty bars represent ±3σ.
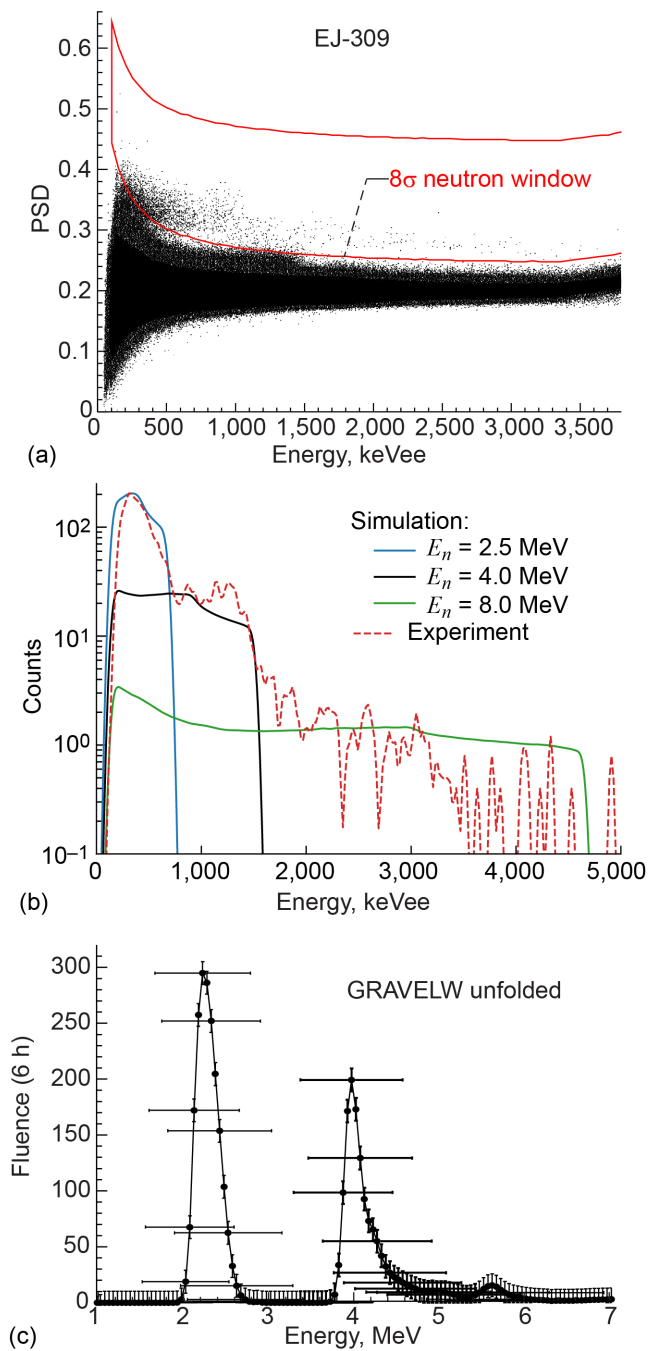
Figure 9.—EJ-309 detector results: (a) experimental pulse shape discrimination (PSD) plot; (b) comparison of simulated monochromatic neutron flux with energies E_n of 2.5 MeV (fusion), 4.0 MeV, and 8.0 MeV spectra versus experimental data from Ref. 6; (c) GRAVELW unfolded spectrum for representative experimental data from Ref. 6 where the uncertainty bars represent ±3σ.

standard check sources (^{137}Cs and ^{60}Co) by fitting a Gaussian distribution, resulting in a σ of 50 keVee. To obtain the plotted 3σ, the original spectrum was "offset" by either +150 keVee or –150 keVee, corresponding to ±3σ on the EJ-309 detector energy resolution (or 120 keVee for the slightly better resolution stilbene detector) prior to unfolding. Then once unfolded, the shifts in the neutron energy peaks (e.g., fusion neutron peak at 2.4 MeV) were determined for both the plus and minus unfolded spectrum. This perturbation analysis resulted in a slightly asymmetric neutron energy uncertainty bar, biased toward the lower energy, as shown in the figures. The fluence uncertainties (vertical bars) were determined using the GRAVELW unfolding methodology using ±3σ (Ref. 23). Note that for clarity, the uncertainty bars were plotted on the figures for only select data points.

6.0   Summary

Organic scintillators with pulse shape discrimination (PSD) capability are widely used in both research and practical applications of neutron detection. The neutron and γ-ray identification performance of the detector depends on the classification algorithms, noise filters and pileup rejection criteria in a high-flux bremsstrahlung radiation environment. In this paper, a technique has been developed and implemented for the neutron detection with multiple filter and discrimination steps, which virtually eliminates counting of γ-ray pulses. Such a technique is merited when making measurements in a high-flux bremsstrahlung and secondary fluorescence environment. The technique developed was benchmarked and calibrated using [252]Cf and Am-Be + [137]Cs sources. The technique was also successfully applied to measure neutron spectra in a high-flux bremsstrahlung environment. For this environment, the PSD boundary between neutrons and γ-rays was set with high confidence by fitting the γ-ray PSD distribution with a Gaussian and setting the edge of the neutron gate as the mean + 8σ (where 8σ corresponds to 1 part in $1.6{\times}10^{15}$). This new technique offers the user the ability to measure neutron spectra in a high-flux γ-ray field and tune the parameters to meet required filtering needs.

References

1. Knoll, Glenn F.: Radiation Detection and Measurement. Fourth ed., John Wiley & Sons, Hoboken, NJ, 2010.
2. Zaitseva, N., et al.: Pulse Shape Discrimination in Impure and Mixed Single-Crystal Organic Scintillators. IEEE Trans. Nucl. Sci., vol. 58, no. 6, 2011, pp. 3411–3420.

3. Eljen Technology: Neutron/Gamma PSD Liquid Scintillator EJ-301, EJ-309. https://eljentechnology.com/images/products/data_sheets/EJ-301_EJ-309.pdf Accessed April 10, 2019.

4. Polack, J.K., et al.: An Algorithm for Charge-Integration, Pulse-Shape Discrimination and Estimation of Neutron/Photon Misclassification in Organic Scintillators. Nucl. Instrum. Methods. Phys. Res. A, vol. 795, 2015, pp. 253–267.

5. Cieślak, M.J.; Gamage, K.A.A.; and Glover, R.: Pulse Shape Discrimination Characteristics of Stilbene Crystal, Pure and 6Li Loaded Plastic Scintillators for a High Resolution Coded-Aperture Neutron Imager. J. Instrum., vol. 12, no. 7, 2017, p. P07023.

6. Steinetz, Bruce M., et al.: Novel Nuclear Reactions Observed in Bremsstrahlung-Irradiated Deuterated Metals. Phys. Rev. C, vol. 101, no. 044610, 2020.

7. Pines, Vladimir, et al.: Nuclear Fusion Reactions in Deuterated Metals. Phys. Rev. C, vol. 101, no. 044609, 2020.

8. CAEN S.p.A.: DT5730 8 Channel 14 Bit 500 MS/s Digitizer. 2019. https://www.caen.it/products/dt5730/ Accessed April 10, 2019.

9. Safari, M.J.; Davani, F. Abbasi; and Afarideh, H.: Differentiation Method for Localization of Compton Edge in Organic Scintillation Detectors. 2016. https://arxiv.org/abs/1610.09185 Accessed April 10, 2019.

10. Enqvist, Andreas, et al.: Neutron Light Output Response and Resolution Functions in EJ-309 Liquid Scintillation Detectors. Nucl. Instrum. Methods. Phys. Res. A, vol. 715, 2013, pp. 79–86.

11. Pino, F., et al.: The Light Output and the Detection Efficiency of the Liquid Scintillator EJ-309. Appl. Radiat. Isot., vol. 89, 2014, pp. 79–84.

12. Cecil, R.A.; Anderson, B.D.; and Madey, R.: Improved Predictions of Neutron Detection Efficiency for Hydrocarbon Scintillators From 1 MeV to About 300 MeV. Nucl. Instrum. Methods, vol. 161, no. 3, 1979, pp. 439–447.

13. Iwanowska, J., et al.: The Time-of-Flight Method for Characterizing the Neutron Response of Liquid Organic Scintillators. Nucl. Instrum. Methods. Phys. Res. A, vol. 781, 2015, pp. 44–49.

14. E. Padovani, et al.: RSICC Code Package CCC–791. https://rsicc.ornl.gov/codes/ccc/ccc7/ccc-791.html Accessed April 10, 2019.

15. Agostinelli, S., et al.: GEANT4—A Simulation Toolkit. Nucl. Instrum. Methods. Phys. Res. A, vol. 506, no. 3, 2003, pp. 250–303.

16. Desplan, Nicolas: Study and Simulation of a BC501A Scintillator. Master's thesis, Stockholm, Sweden, 2013.

17. Mannhart, W.: Evaluation of the Cf-252 Fission Neutron Spectrum Between 0 MeV and 20 MeV. International Atomic Energy Agency, 1987. https://inis.iaea.org/search/search.aspx?orig_q=RN:18075519 Accessed May 16, 2019.

18. Gonnenwein, F.: Neutron and Gamma Emission in Fission. Presented at the LANL FIESTA Fission School & Workshop, Santa Fe, NM, 2014. https://t2.lanl.gov/ fiesta2014/school/Goennenwein.pdf Accessed April 10, 2019.

19. Bourne, M.M., et al.: Neutron Detection in a High-Gamma Field Using Solution-Grown Stilbene. Nucl. Instrum. Methods. Phys. Res. A, vol. 806, 2016, pp. 348–355.

20. Baramsai, B., et al.: Characterization and Testing of EJ-309 and Stilbene Scintillation Detectors. Proceedings of Hard X-Ray, Gamma-Ray, and Neutron Detector Physics XVII, SPIE 9593, 2015. https://doi.org/10.1117/12.2192436 Accessed April 10, 2019.

21. Saldana, Luis; and Stemen, Nate: Pulse Shape Discrimination Methods. 2014. https://wlab.yale.edu/sites/default/files/psdpresentation.pdf Accessed April 10, 2019.

22. Iwanowska-Hanke, Joanna, et al.: Comparative Study of Large Samples (2" × 2") Plastic Scintillators and EJ309 Liquid With Pulse Shape Discrimination (PSD) Capabilities. J. Instrum., vol. 9, no. 6, 2014, p. P06014.

23. Matzke, Manfred: The HEPROW Program System. http://matzke-bs.de/heprow/Dateien/HEPROW.PDF Accessed April 10, 2019.